Fuel 409 (2026) 137792

Contents lists available at ScienceDirect

Fuel

journal homepage: www.elsevier.com/locate/fuel

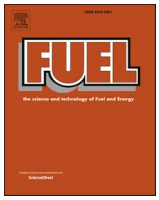

Full Length Article

Radiometer measurements of the spectrally resolved radiative heat flux in a combustion chamber☆

L. Pörtner [a,*], B. Özer [b], D. König [c], M. Richter [c], M. Schiemann [a], A. Maßmeyer [b], J. Ströhle [c], B. Epple [c]

[a] Ruhr University Bochum, Faculty of Mechanical Engineering, Institute for Energy Plant Technology (LEAT), Universitätsstraße 150, 44801 Bochum, Germany
[b] RWTH Aachen University, Faculty of Mechanical Engineering, Institute of Heat and Mass Transfer (WSA), Augustinerbach 6, 52056 Aachen, Germany
[c] TU Darmstadt, Faculty of Mechanical Engineering, Institute for Energy Systems & Technology (EST), Otto-Berndt-Straße 2, 64287 Darmstadt, Germany

ARTICLE INFO

Keywords:
Biomass
Optical measurement
Heat flux
Ellipsoidal radiometer
Oxy-fuel
Gas species

ABSTRACT

So far ellipsoidal radiometers used in combustion environments have been limited to broadband measurements of total radiative intensity, converting the total incident thermal radiation into an integral electrical voltage signal while neglecting information about the incident radiation's wavelength distribution. To preserve this spectral information, the novel radiometer concept presented in this study enables spectrally resolved radiative heat flux measurements inside a combustion chamber. For this purpose, the established design of ellipsoidal hemispheric radiometer cavities was extended by integrating hollow optical fibers as radiation guides. This combination allows the use of radiation analysis instruments, such as a Fourier transform infrared spectrometer, outside the chamber. Calibration measurements were conducted to determine the angular-dependent response of the radiometer and to perform a wavelength-resolved intensity calibration. These procedures enable a reliable interpretation of the collected radiation signals within the combustion chamber. Furthermore, the radiometer was applied at an oxyfuel-driven laminar flow reactor and a 1MWth test facility, investigating three different pulverized walnut shell flames – one under air and two under oxyfuel conditions. The obtained results allowed the identification of emission lines from water vapor, carbon dioxide and methane, emission lines, as well as radiative heat flux distributions at different measurement positions within the combustion chamber. Based on these distributions, an influence of radiation absorption effects related to varying gas temperature profiles inside the combustion chamber were observed.

1. Introduction

The behavior of a combustion system strongly depends on its individual heat transfer characteristics, which, in the most common case of turbulent combustion, are dominated by convection and radiation. For a comprehensive description of such a system, its radiative properties are of fundamental importance. In addition to the contribution of radiation to the overall heat transfer, the spectral distribution of the emitted radiation provides valuable information about the ongoing combustion processes. Consequently, a detailed understanding of the radiative properties is essential for an accurate characterization of a combustion system.

Since the total radiative heat flux represents the amount of energy transferred per unit time to a surface element by radiation, it is the key parameter for radiative heat transfer system characterization [1–4]. The total radiative heat flux is commonly determined using ellipsoidal radiometers. These instruments are typically designed as probes that can be inserted into the combustion chamber and consist of an ellipsoidal cavity with an opening at one focal plane of the ellipse and a radiation-sensitive detector at the other. However, the specific design may vary depending on the application.

Using such a radiometer, Smart et al. [3] investigated the total radiative heat flux of various coal and coal-biomass co-fired flames under air-firing and oxyfuel conditions, covering eight different chamber wall positions at varying distances to the burner. A MEDTHERM radiative heat flux sensor was employed to detect the radiation incident on the front hemisphere of the radiometer via its ellipsoid cavity and thermopile detector. Based on the acquired radiation data, dependencies of the radiative heat transfer on the oxygen concentration in the

☆ This article is part of a special issue entitled: 'Oxyflame-5' published in Fuel.

* Corresponding author.
E-mail address: poertner@leat.rub.de (L. Pörtner).

https://doi.org/10.1016/j.fuel.2025.137792
Received 16 June 2025; Received in revised form 13 October 2025; Accepted 28 November 2025
Available online 2 December 2025

Nomenclature

a_i	Radiometer intensity correction factor for spectrometer channel i
α	Incident radiation angle
b_i	Corrected radiometer intensity correction factor for spectrometer channel i
i	Spectrometer channel index
$\overline{I_{BG_i}}$	Average measured background radiation intensity at spectrometer channel i
$\Delta\overline{I_{BG_i}}$	Uncertainty of $\overline{I_{BG_i}}$
I_{Meas_i}	Background reduced measured lamp radiation intensity at spectrometer channel i
ΔI_{Meas_i}	Uncertainty of the background reduced measured lamp radiation intensity at spectrometer channel i
$\overline{I_{L_i}}$	Average measured lamp radiation intensity at spectrometer channel i
$\Delta\overline{I_{L_i}}$	Uncertainty of $\overline{I_{L_i}}$
I_{Orig_j}	Original lamp spectrum radiation intensity at wavelength λ_{Orig_j}
I_{Ref_i}	Spectrometer reference intensity of channel i
j	Original lamp spectrum wavelength index
$\lambda_{MIR\,i}$	Spectrometer center wavelength of channel i
λ_{Orig_j}	Original lamp spectrum wavelength with index j

Abbreviations & Subscripts:

FTIR	Fourier transformation infrared
LFR	Laminar flow reactor
PMT	Photomultiplier
wt	weight

Similar results were reported by Corrêa da Silva et al. [4], who determined the total radiative heat flux of lignite-fired flames under various oxyfuel and air-firing conditions at the chamber wall. The heat flux measurements were conducted using a thermopile-based ellipsoidal radiometer with a cavity featuring a gold-coated cavity to enhance surface reflectivity and small ports for N_2-purge gas injection.

An similar approach was first applied by Maßmeyer et al. [5] and later adopted by Zabrodiec et al. [6]. They investigated the total radiative heat flux in a 60 kW_{th} combustion chamber at different chamber wall positions for coal, Rhenish lignite and torrefied biomass flames under both air-firing and oxyfuel conditions. Compared to the radiometer used by Corrêa da Silva et al. [4], the elliptic cavity of the radiometer manufactured by Green Flames Technology featured a window at the cavity center, to further protect the thermopile from combustion deposits. Their results also showed higher heat fluxes under air-firing conditions compared to oxyfuel atmospheres, as well as variations in flame geometry depending on the operation conditions.

A detailed characterization of a thermopile-based ellipsoidal radiometer was provided by Murthy et al. [7] whose investigations examined the radiometer's response as a function of the incident radiation angle and its distance from the radiation source. The angular response measurements revealed asymmetrical radiation intensity distributions within the ± 40° range around the 0° incident angle, which were attributed to non-uniform reflection from the gold-plated cavity surface. The source-distance-dependent responsivity of the radiometer was determined through transfer calibration and exhibited an initial decrease of approximately 10 %, followed by a gradual increase. This variation was attributed to the narrow view-angle calibration method, typically used for narrow-angle radiometers [8]. In addition, the influence of the applied argon purge gas flow on the measurement results was analyzed. A nearly linear decrease in signal output with increasing flow rate was observed. However, for flow rates below 0.001 m^3/s, the signal reduction remained below 1 %.

As demonstrated by the publications mentioned above, the use of

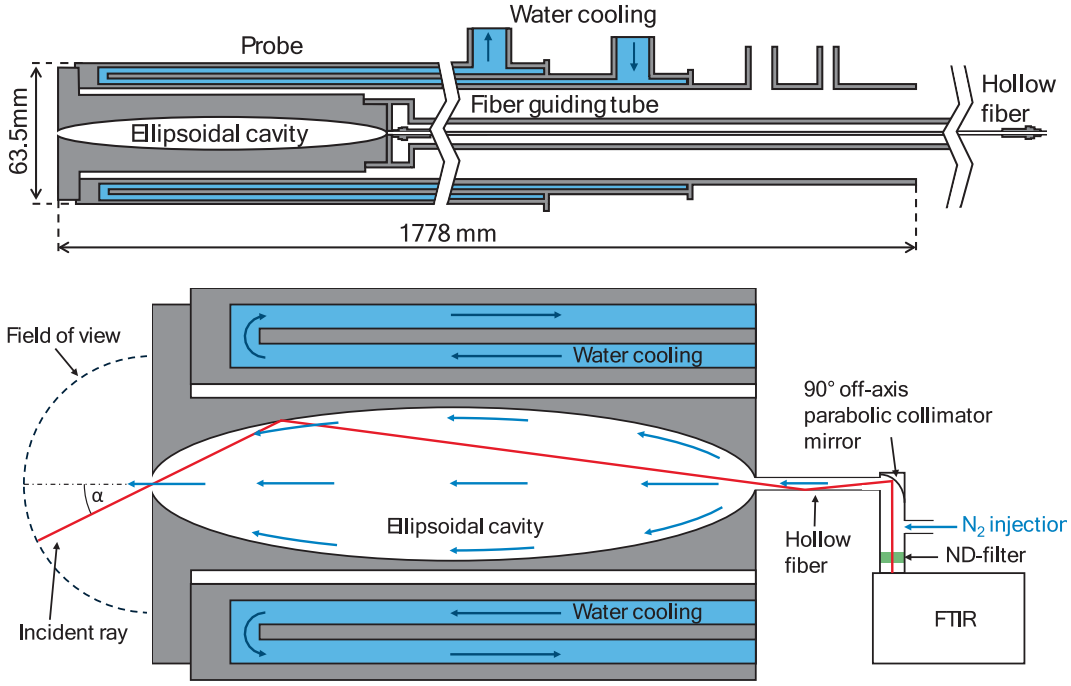

Fig. 1. Radiometer probe design (top) with radiation guiding and purge flow concept (bottom).

combustion atmosphere as well as on the fuel type and composition were identified, as these parameters influence both flame temperature and geometry.

ellipsoidal radiometers for combustion chamber characterization is well established. Due to their geometry, ellipsoidal cavities at the radiometer inlets provide a wide field of view, focusing the incident radiation onto

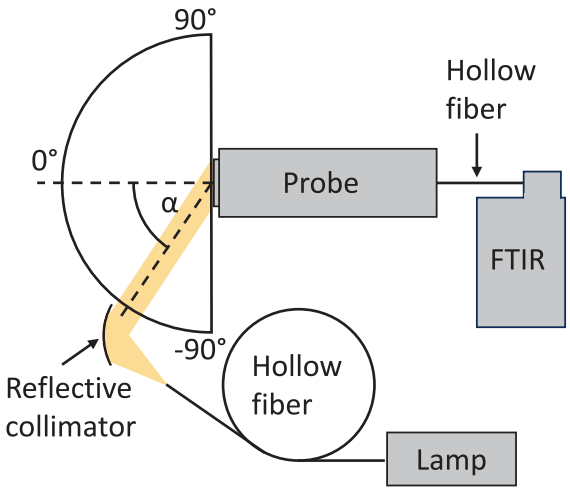

Fig. 2. Radiometer responsivity measurement setup.

the sensor. Moreover, the use of thermopiles as radiometer detectors is well established, as these sensors are sensitive across a broad wavelength range. However, they have so far been limited to broadband total radiative intensity measurements, since they convert the total incident thermal radiation into an integrated electrical voltage signal. Consequently, spectral information about the incident radiation is lost when thermopile detectors are applied.

Preserving this information, however, is crucial for identifying correlations between measured radiation intensity distributions and various combustion parameters. These include the determination of gaseous species concentrations (e.g. of CO_2), as well as gas or particle temperature and total effective emissivity [8–14]. Furthermore, this spectral information can serve as a basis for theoretical simulations and modeling approaches as demonstrated in [15,16], where strong wavelength dependencies of the spectral absorption and scattering efficiencies of fuel and ash particles were considered. Additionally, wavelength-resolved data may also allow the identification of radiation effects associated with chamber wall or combustion deposits, as reported in [17].

Since the dimensions of the setup used for this type of analysis are not suitable for probe integration, Tree et al. [8] and Adams et al. [9] guided the radiation from the combustion chamber to the analysis setup via optical fibers. Building upon this approach, the radiometer developed in the present study combines the radiation collection capability of an ellipsoidal cavity with optical fiber radiation guiding. This design enables the use of external radiation analysis instruments while maintaining a wide observation field of view.

Spectrally resolved radiative heat flux are scarcely reported in literature, although their relevance for process understanding and model validation is unquestionable. Therefore, a novel radiometer was developed to extend the concept of an ellipsoidal cavity from spectrally integrating detectors (state-of-the-art) to detectors providing spectral resolution. The radiometer was specifically designed and calibrated to investigate differences in radiative heat flux within a semi-industrial combustion chamber. This study demonstrates the capabilities and limitations of the developed radiometer, as well as the effects of operating conditions on the measured radiative heat flux. The resulting data provide initial insights into the interplay between gas absorption and emission phenomena, which can serve as a basis for modelling under varying thermal and species conditions.

2. Radiometer

2.1. Design and measurement concept

The radiometer's design extends the principle of the ellipsoidal radiometer probe by incorporating optical fiber radiation guiding. Incident radiation from nearly all directions within the radiating domain enters the cavity through its aperture, located at one focal plane of the enclosing ellipse. After a single reflection on the cavity surface, or via a direct optical path, the radiation is directed toward the cavity exit, which is symmetrically positioned at the second focal plane of the ellipse. Instead of integrating a thermopile-based sensor at this position, an optical fiber is coupled to the cavity, transmitting the collected radiation from the combustion chamber to the external detector setup. A schematic of the probe design, along with the radiation guiding and purge flow concept, is shown in Fig. 1.

Due to symmetry considerations, the properties of the fiber applied determine the cavity dimensions. Incident radiation from all directions entering the cavity illuminates an area at the exit focal plane that matches the dimensions of the entrance aperture. Consequently, the cavity entrance and exit apertures are designed to be of equal size. To minimize radiation losses when coupling the cavity to the optical fiber, the aperture dimensions are matched to the fiber diameter.

A hollow-core fiber was selected for its advantages, particularly in the experimental setup employed in this study. Compared to solid-core fibers, this hollow fiber exhibits a higher acceptance angle, resulting from the absence of a medium transition for the incident radiation. Moreover, its large core diameter allows for relatively large cavity apertures, thereby maximizing the collected radiation intensity. In addition, the hollow fiber enables the application of a nitrogen purge flow through both the fiber and the cavity, avoiding the need for additional inlets in the cavity surface that would otherwise lead to radiation losses.

The hollow-core fiber used in this study (manufactured by Guiding Photonics) has a length of 2 m and a core diameter of 1.5 mm. An inner high-reflectivity coating for the wavelength range of 2–10 μm (Type SWMW) minimizes infrared radiation losses. The cavity has a major axis of 150 mm and a minor axis of 15 mm and is coated with gold to further enhance infrared reflectivity and reduce radiation losses.

The detector employed in this study is a fiber-coupled MIR-FTIR spectrometer (ARCoptix Rocket FTMIR-L1-060-4TE) equipped with a reflective fiber coupler/collimator, operating in the wavelength range of 2–6 μm. The reflective fiber coupler contains a 90°off-axis parabolic mirror with an aligned fiber port. An extension of the mirror mount was incorporated to enable the installation of a neutral density (ND) filter with 10 % transmittance in the infrared region. This ND filter prevents saturation of the spectrometer detector during combustion chamber measurements.

For combustion chamber measurements, the instrumentation must be protected from combustion products. To ensure this, a nitrogen purge flow is introduced via the spectrometer mirror mount extension into the measurement system. The nitrogen flows through the hollow-core fiber into the ellipsoidal cavity and exits the probe through the cavity entrance into the combustion chamber. Leakage of this flow into the spectrometer is prevented by the inserted ND-filter and a protective entrance window. It should be noted that the nitrogen has no effect on the measured spectrum, as it exhibits no absorption or emission lines in the spectral region of interest.

To maintain stable operation conditions, the probe is equipped with water cooling, preventing overheating of all components and minimizing measurement artifacts caused by self-emitted radiation. Matching the access port dimensions and overall system size of the 1 MW_{th} combustion chamber discussed later, the radiometer probe was designed with a diameter of 63.5 mm and a length of 1.778 m, excluding the attached radiation analysis setup consisting of the collimator and FTIR spectrometer.

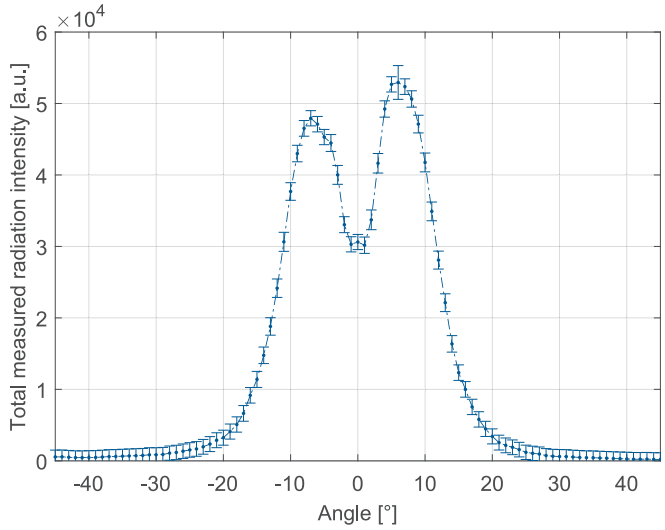

Fig. 3. Radiometer responsivity in dependence of the incident radiation angle in the reduced regime of α = -45° to α = 45°.

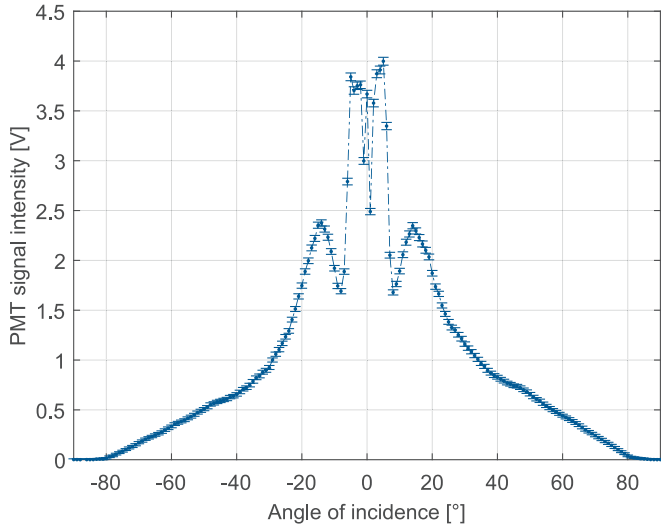

Fig. 4. Measured angular dependent transmitted radiation intensity of the elliptic cavity, detected by a photomultiplier at the cavity exit surface.

2.2. Angular-dependent responsivity

Accurate interpretation of the experimental results requires detailed knowledge of the spectrometer characteristics, particularly its directional and spectral response. A schematic of the setup used to determine these radiometer characteristics is shown in Fig. 2.

A stabilized broadband tungsten lamp (Thorlabs SLS202L), emitting radiation in the wavelength range of 450–5500 nm with an optical power maximum of 700 mW, was coupled to a hollow-core fiber identical to that used in the radiometer. At the end of the fiber, a reflective collimator (Thorlabs RC02SMA-P01) produced a parallel radiation beam with an approximated diameter of 5 mm. The collimator was mounted on a rotation stage to direct the tungsten lamp radiation to the entrance of the radiometer. With the radiometer entrance aligned with the rotation axis, the incident angle of the collimated radiation was varied between α = -90° and α = 90° in steps of 1°.

For each irradiation angle, 100 spectra of the lamp and background radiation were recorded. The angular response function was determined by averaging and integrating the 100 spectra, followed by background subtraction. Reduced for clarity, the results of angles between α = -45° and α = 45° are displayed in Fig. 3.

The measured signal intensity distribution exhibits an almost symmetrical behavior. Starting from 0°, corresponding to direct radiation transfer through the cavity without reflection, the intensity initially decreases slightly, reaching a minimum at α = +/-1°. It them increases by approximately 30 % to a maximum at around α = +6°/-7°, before gradually decreasing to zero at approximately α = +/-40°.

The symmetrical distribution is typical for elliptic radiometers, as similar behavior was reported in [7]. However, the reduced intensity at α = 0° compared to the maximum at α = +6°/-7° is attributed to imperfect collimation of the incident radiation, resulting in radiation losses. For perfectly collimated radiation, a peak at α = 0° would be expected. In addition, low incident angles lead to large fiber coupling angles, which also contribute to radiation losses. Surface roughness of the cavity may further reduce the transmitted radiation, as the cavity was manufactured in the institute workshop and does not meet standard optical surface quality requirements. Moreover, the sputtered gold layer on the cavity surface is assumed to be irregular, since both cavity halves were held at varying plasma distances during deposition. Finally, as discussed in [7], a wider, cosine-like distribution of the received intensity profile would be expected.

To characterize the properties of the elliptic cavity, the setup shown in Fig. 2 was modified by replacing the radiometer's spectrometer and hollow-core fiber with a photomultiplier (PMT; Hamamatsu PMT H10723-20), sensitive over the wavelength range of 230–920 nm. Due to the PMT's operational wavelength range, the hollow-core fiber connected to the tungsten lamb was replaced with a fiber matching the PMT properties (Thorlabs FG910LEC, length 1 m). This fiber was selected for its high transmissivity in the wavelength range of 400–2200 nm, overlapping with the PMT sensitivity, and its core diameter of 910 μm, for a maximized transmitted radiation intensity.

The angular dependence measurements were then repeated using the modified setup. The incident angle of the radiation was varied in 1° increments from α = -90° to α = 90°. The resulting electrical voltage signal distribution is shown in Fig. 4.

The measured signal intensity exhibits a pronounced angular sensitivity between α = 80° and α = -80°, symmetrically centered around α = 0°. No radiation was detected for angles between α = 80° and α = 90°. The prominent peak at α = 0° corresponds to radiation transmitted through the cavity without interaction with its walls. Due to imperfect collimation of the radiation from the fiber-coupled tungsten lamp, some incident radiation at α = 0° is partially blocked near the cavity exit and not fully transmitted. As these results are in closer agreement with the observations reported in [7] than with those shown in Fig. 3, it can be concluded that fiber coupling and the use of the MIR spectrometer in the previous setup are responsible for substantial radiation intensity losses.

2.3. Wavelength dependent radiation intensity calibration

Since all radiometer components exhibit wavelength-dependent reflectivity and sensitivity, calibration is required to obtain wavelength-resolved total intensity distributions that accurately represent the incident radiation. For this purpose, the stabilized broadband tungsten lamp (Thorlabs SLS202L) was focused onto the entrance aperture of the radiometer. Subsequently, 100 spectra of the lamp and the corresponding background radiation were recorded. After averaging the respective spectra to obtain $\overline{I_{L_i}}$ and $\overline{I_{BG_i}}$ with their standard deviations $\Delta\overline{I_{L_i}}$ and $\Delta\overline{I_{BG_i}}$ representing the measurement uncertainties, the lamp spectrum is calculated as:

$$I_{Meas_i} = \overline{I_{L_i}} - \overline{I_{BG_i}} \tag{1}$$

The corresponding uncertainty is obtained by applying Gaussian error propagation, expressed as:

$$\Delta I_{Meas_i} = \sqrt{\left(\Delta\overline{I_{L_i}}\right)^2 + \left(-\Delta\overline{I_{BG_i}}\right)^2} \tag{2}$$

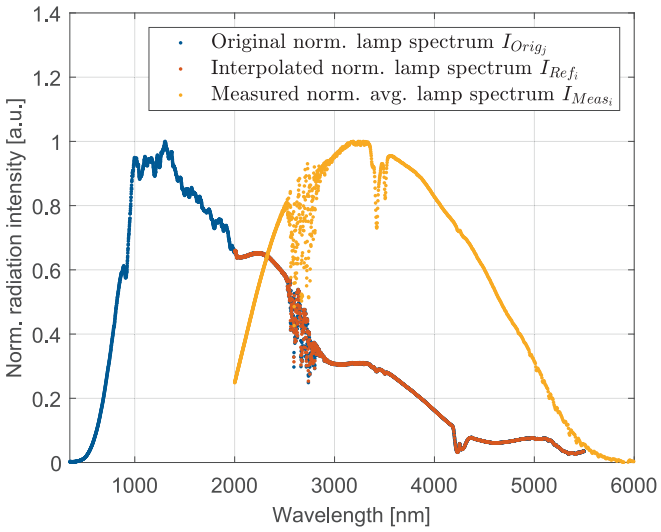

Fig. 5. Original, interpolated and measured lamp spectrum.

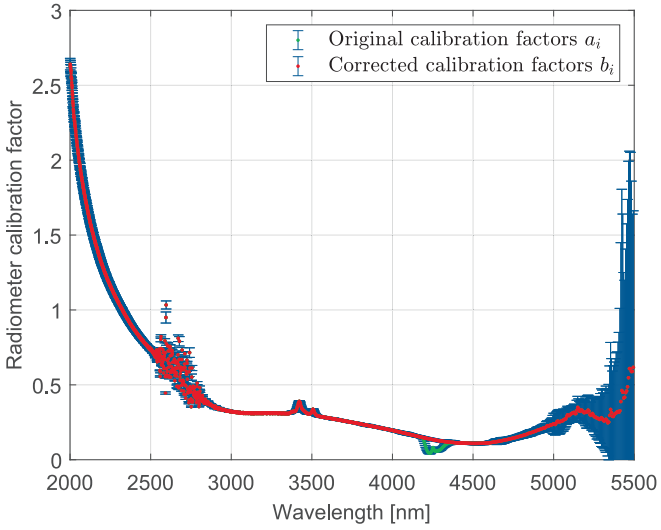

Fig. 6. Original radiometer measurement radiation intensity calibration factors a_i and CO_2 influence corrected calibration factors b_i.

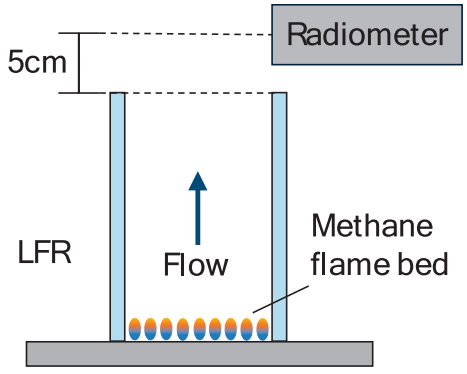

Fig. 7. Laminar flow reactor exhaust gas radiation analysis setup.

In the next step, the measured spectrum intensities are compared with the lamp spectrum intensities I_{Orig} provided by the manufacturer. Since the lamp spectrum is available only in the wavelength range of 0.35–5.5 µm, both spectra are normalized to their respective maximum values within this region. Moreover, the spectral resolution of the lamp spectrum does not coincide with the central channel wavelengths of the MIR spectrometer. Consequently, the corresponding reference intensity I_{Ref_i} for each MIR spectrometer wavelength λ_{MIR_i} is determined by linear interpolation between the two adjacent original lamp spectrum intensities I_{Orig_j} and $I_{Orig_{j+1}}$ at the closest lamp spectrum wavelengths λ_{Orig_j} and $\lambda_{Orig_{j+1}}$,according to:

$$\lambda_{Orig_j} < \lambda_{MIR_i} < \lambda_{Orig_{j+1}} \tag{3}$$

Subsequently, the corresponding interpolated reference intensities I_{Ref_i} are obtained as:

$$I_{Ref_i} = I_{Orig_j} + \frac{\lambda_{MIR_i} - \lambda_{Orig_j}}{\lambda_{Orig_{j+1}} - \lambda_{Orig_j}} \left[I_{Orig_{j+1}} - I_{Orig_j} \right] \tag{4}$$

The corresponding curves are shown in Fig. 5.

By determining the ratio between the interpolated original lamp spectrum and the background-corrected measured spectrum, the radiometer calibration factors for each wavelength are obtained as:

$$a_i = \frac{I_{Ref_i}}{I_{Meas_i}} \tag{5}$$

The uncertainties of the calibration factors were calculated using Gaussian error propagation as:

$$\Delta a_i = \sqrt{\left(-\frac{\Delta I_{Meas_i}}{(I_{Meas_i})^2} \right)^2} \tag{6}$$

The determined calibration factors are shown in Fig. 6.

Before activating the N_2 purge flow, fluctuating artefacts were observed in the measured lamp spectrum between 4.18–4.39 µm. These artefacts also appear in the manufacturer-provided lamp spectrum and were attributed to the presence of CO_2 during the manufacturer's measurements. Upon switching on the radiometer's N_2 flow, which is mandatory for combustion chamber experiments, the two dips disappeared as the purge flow displaced the previously present CO_2. This supports a correction of the determined calibration factors in this spectral range.

Since the measured spectrum exhibits a continuous decreasing trend from 4.18-4.39 µm, the original lamp spectrum is assumed to follow the same trend. Accordingly, a 7th-degree polynomial was fitted to the 177 correction factors in the spectral regions 3.8–4.18 µm and 4.37–4.6 µm to best match the determined data, achieving $R^2 > 0.99996$. As the uncertainty of the radiometer measurements was assumed constant in the replaced region, the uncertainties of the corrected calibration factor curve were taken equal to the original calibration factors. The resulting corrected radiometer calibration factors b_i were then applied in the subsequent analysis.

Table 1
Laminar flow reactor atmosphere composition input and exhaust gas composition calculated from the input gas composition.

Input [ln/min]			Exhaust [mol/mol %]		
CH_4	O_2	CO_2	O_2	CO_2	H_2O
3.07	13.16	20.51	19.1	64.2	16.7

3. Laminar flow reactor exhaust gas radiation analysis

To verify the measurement principle and assess the radiometer's functionality, initial tests were conducted at the exhaust gas outlet of a methane-driven laminar flow reactor (LFR) previously described in [18–20]. As shown in Fig. 7, the probe tip center was positioned within

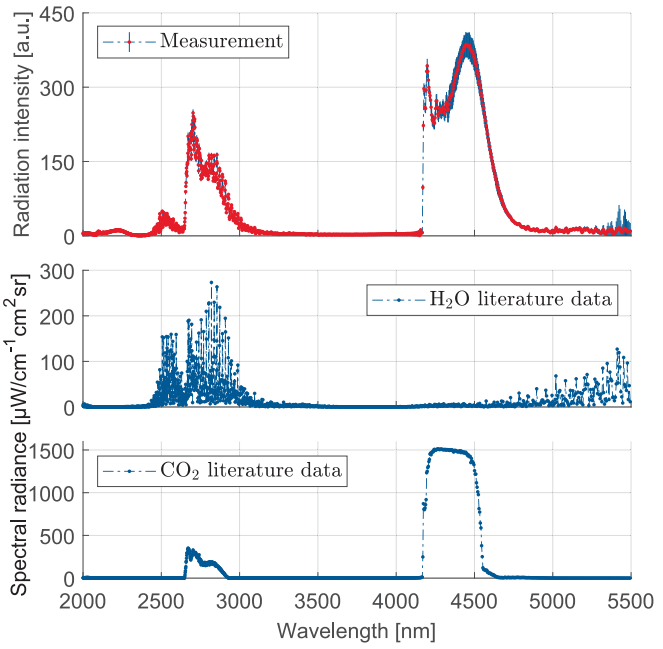

Fig. 8. Determined laminar flow reactor exhaust gas emission spectrum (top) with species peaks of H_2O (middle) and CO_2 (bottom) from [21,22].

the exhaust gas stream, 5 cm above the burner's flue gas outlet. The reactor was operated under an oxyfuel atmosphere, for which the resulting exhaust gas is known to consist solely of H_2O, O_2 and CO_2. Detailed information on the reactant composition and resulting exhaust gas flow is provided in Table 1.

Subsequently, 100 individual spectra were recorded with the radiometer and averaged. To account for potential contributions from thermal radiation of the reactor glass tube wall, a background measurement was performed in the same manner after the burner was shut down. The exhaust gas radiation spectrum was obtained by subtracting this background. The resulting spectrum was then compared with literature emission spectra of the participating gas species H_2O and CO_2, calculated using SpectraPlot.com [21] based on the data from [22]. Following previous investigations by Tarlinski et al. [23], the exhaust gas temperature was assumed to be 1400 K. The species mole fractions were set according to the gas composition presented in Table 1, with $X_{H2O} = 0.167$ and $X_{CO2} = 0.642$. The pressure was set to standard atmospheric conditions, and the optical path length was taken as 5 cm, corresponding to the reactor's exhaust dimensions. The resulting exhaust gas and species emission spectra are presented in Fig. 8.

Table 2
Combustion atmospheres.

Atmosphere	Thermal Power [kW_{th}]	Composition [$\%_{vol}$]			
		O_2	N_2	CO_2	H_2O
Air	420	21	79	0	0
Oxy-RECY	420	33	20	37	10
Oxy-DRY	420	33	0	67	0

Table 3
Fuel analysis.

Ultimate analysis				Proximate analysis			
Component	wt.-%, dry			Component	wt.-%, dry		
C	47.61	±	0.03	Fixed carbon	11.30	±	0.49
H	6.04	±	0.04	Volatile matter	80.86	±	0.25
S	0.00	±	0.00	Moisture	7.14	±	0.20
N	0.36	±	0.01	Ash	0.70	±	0.04
O*	45.99	±	0.08				

* Calculated by difference.

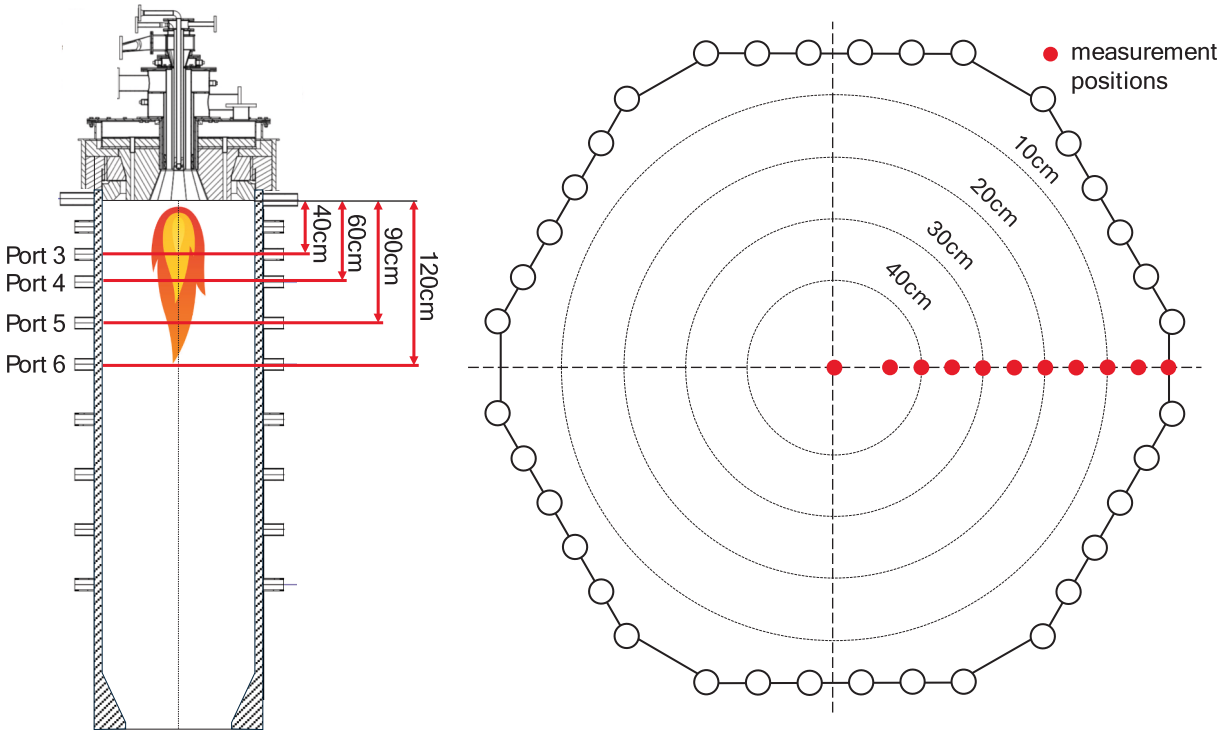

Fig. 9. Vertical combustion chamber cross-section including burner, measurement ports and measurement level (left). Horizontal combustion chamber cross section at measurement level including measurement positions (right).

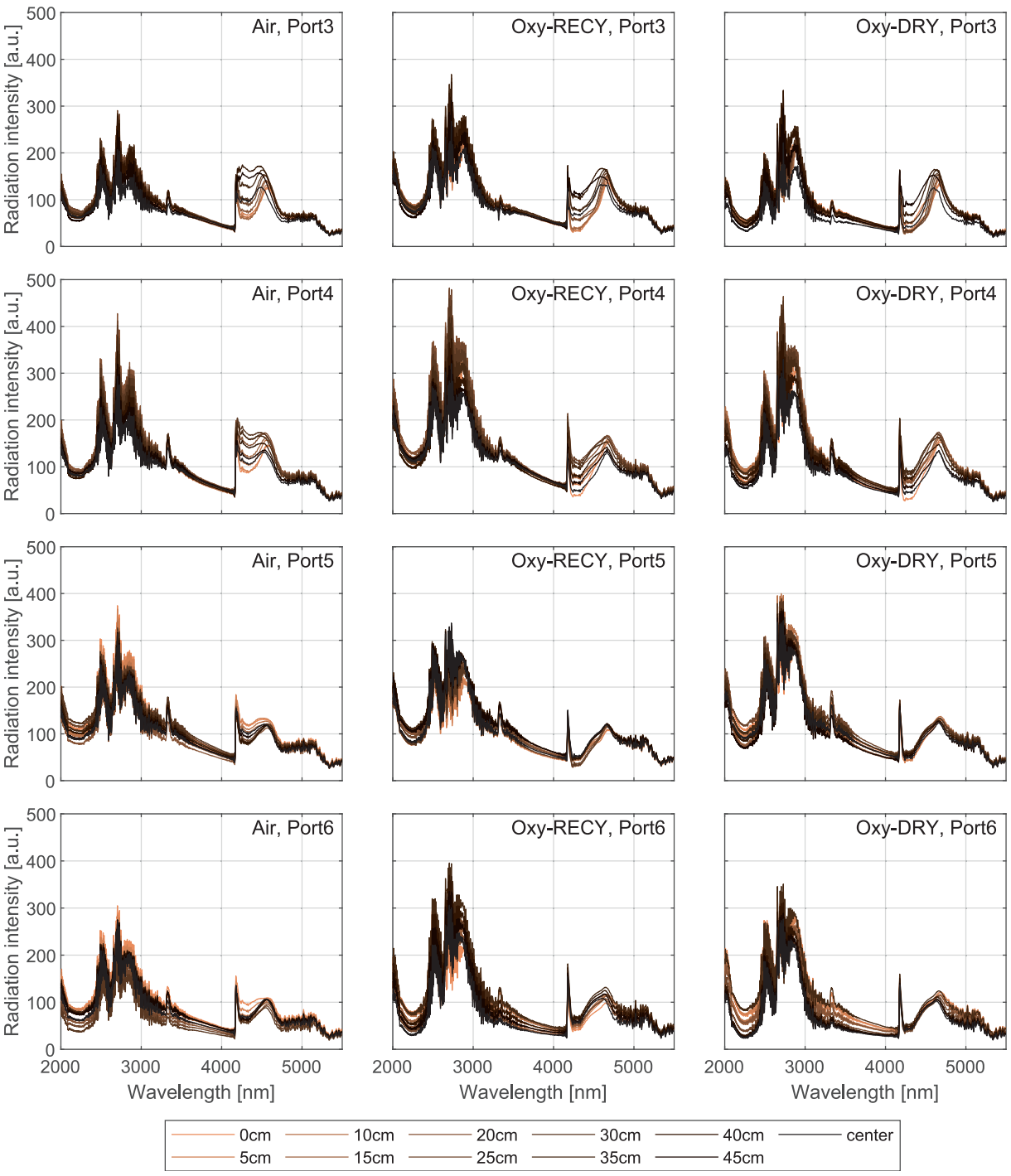

Fig. 10. Measured spectrums of three different atmospheres (Air, Oxy-RECY, Oxy-DRY), four ports (3–6) and eleven axial positions.

It should be noted that the units of the measured radiation intensities in this study are given in arbitrary units ([a.u.]), as determining absolute intensities would require a reference measurement, which could not be performed due to dimensional constraints of the radiometer probe and the available reference radiator. This issue will need to be addressed in future investigations. Furthermore, the literature data obtained from [21] had a wavelength resolution differing from that of the radiometer measurements. To improve comparability, the literature data were processed to match the radiometer's spectral resolution. Each data point of the literature data was assigned to the closest radiometer wavelength, and the spectral radiance values corresponding to each radiometer wavelength were subsequently averaged.

The measured gas radiation spectrum exhibits two regions of emitted radiation, spanning 2.4–3.3 μm and 4.1–5 μm. Since the primary radiation-emitting exhaust gas species are known to be H_2O and CO_2, the observed peaks can be attributed to these species based on the corresponding literature data, shown in the center (H_2O) and bottom (CO_2) diagrams.

However, the measured peak intensity distributions differ from the literature data. For water vapor, the wavelength range of the emission matches the measured region, but the relative peak intensities at 2.53 μm and 2.7 μm differ from the literature data. This discrepancy is likely due to overlapping CO_2 emission, as the CO_2 spectrum also exhibits peaks in the 2.66–2.9 μm range. Consequently, the measured radiation

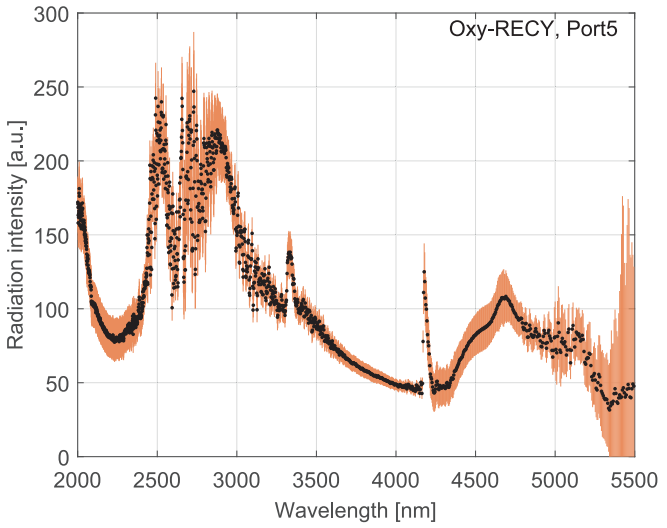

Fig. 11. Exemplary measured spectrum under Oxy-RECY condition at port 5 at wall position including the measurement uncertainties.

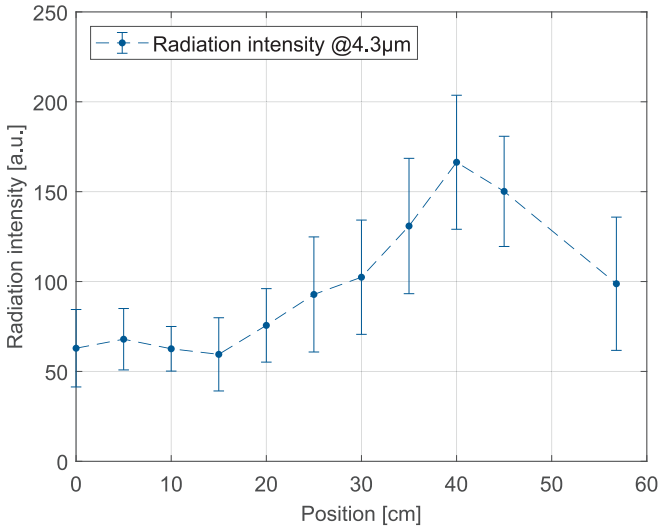

Fig. 12. Measurement position dependent radiation intensity distribution at a wavelength of 4.3 µm at port 3 of the air atmosphere.

between 2.4–3.3 µm is likely a superposition of H_2O and CO_2 radiation emissions, with relatively high contribution from CO_2.

In the 4.1–5 µm region, which is also attributed to CO_2 radiation emission, the measured intensities are lower and differ in distribution compared to the literature data. Although not apparent in the figure, the wavelength range of the measured radiation corresponds to the literature data, however, the literature intensity in the higher regions up to 4.7 µm is extremely low. This observation, together with the local intensity minimum near 4.25 µm, suggests presence of radiation absorption by cold CO_2. This cold CO_2 could have been entrained into the exhaust stream from the surrounding atmosphere via the Venturi effect, as the measurements were taken above the reactor walls, or the lab atmosphere contained CO2 which was not aspired efficiently enough. Furthermore, the CO_2 absorption spectrum has a narrower spectral distribution than the emission spectrum [22], which could account for the local minimum observed in the measured radiation intensities.

4. Measurements in a solid fuel flame combustion chamber

4.1. Combustion chamber and measurement positions

The next radiometer measurements were conducted in a 1 MW_{th} top-fired vertical furnace located at TU Darmstadt [2,24,25]. The combustion chamber is equipped with a swirl burner and enclosed by water-cooled walls, so that heat transfer to the walls is predominantly due to thermal radiation. The upper part of the furnace has a hexagonal cross-section, with an inner distance of approximately 1.1 m between opposite corners and a length of 4 m. 36 measurement ports are located at the chamber corners at various axial distances from the burner to accommodate measurement equipment.

For the radiometer measurements, four different ports were selected, corresponding to measurement heights of 40, 60, 90 and 120 cm beneath the burner plane, and eleven radial injection depth, defined by the position of the radiometer entrance aperture. The measurement positions were evenly distributed relative to the chamber wall in 5 cm increments between the wall and the chamber center, with the exception of the central position. Vertical and horizontal cross-sections of the combustion chamber, including markers for the performed measurement positions and the fixed measurement heights, are presented in Fig. 9.

4.2. Operating conditions

For the current measurement campaign, three different walnut shell solid fuel flames were analyzed. The radiation measurements presented in this work were conducted during a test run of the combustion chamber, aimed at comparing one air-fired and two oxyfuel flames. The two oxyfuel flames differ in their composition, since the Oxy-RECY flame is based on recirculated flue gas, whereas the Oxy-DRY flame is mixed from pure O_2 and CO_2 synthetically. Compared to air flames, the higher oxygen concentration in the oxyfuel flames was chosen to compensate for the temperature-lowering and combustion-inhibiting effects if the elevated CO_2 content in the oxyfuel atmosphere. A detailed description of the operating conditions and the analysis results of the fired fuel can be found in Table 2 and Table 3.

4.3. Results and Discussion

For all previously described radiometer measurement positions and combustion atmospheres, 100 individual spectra were recorded. To minimize the influence of the radiometer temperature, which increases with insertion depth and recording time, the radiometer was removed from the chamber between each measurement position. In addition, a background measurement consisting of 100 individual spectra was performed while the probe remained mounted at the chamber but was isolated from the combustion volume by a cold ball valve.

The 100 recorded spectra for each measurement position and atmosphere, as well as the corresponding background measurements, were averaged to obtain mean values $\overline{I_{C_i}}$ and $\overline{I_{BG_i}}$, with their respective uncertainties $\Delta\overline{I_{C_i}}$ and $\Delta\overline{I_{BG_i}}$, defined as the standard deviation. The resulting mean spectra were then background-corrected and multiplied by the wavelength-dependent corrected calibration factors obtained from the preceding calibration.

$$I_{Meas_i} = \left(\overline{I_{C_i}} - \overline{I_{BG_i}}\right) b_i \tag{7}$$

The corresponding uncertainty was determined using Gaussian error propagation as:

$$\Delta I_{Meas_i} = \sqrt{\left(b_i \Delta\overline{I_{L_i}}\right)^2 + \left(-b_i \Delta\overline{I_{BG_i}}\right)^2 + \left(\left(\overline{I_{C_i}} - \overline{I_{BG_i}}\right)\Delta b_i\right)^2} \tag{8}$$

The resulting spectra are shown in Fig. 10.

For improved clarity, the measurement uncertainties are omitted in

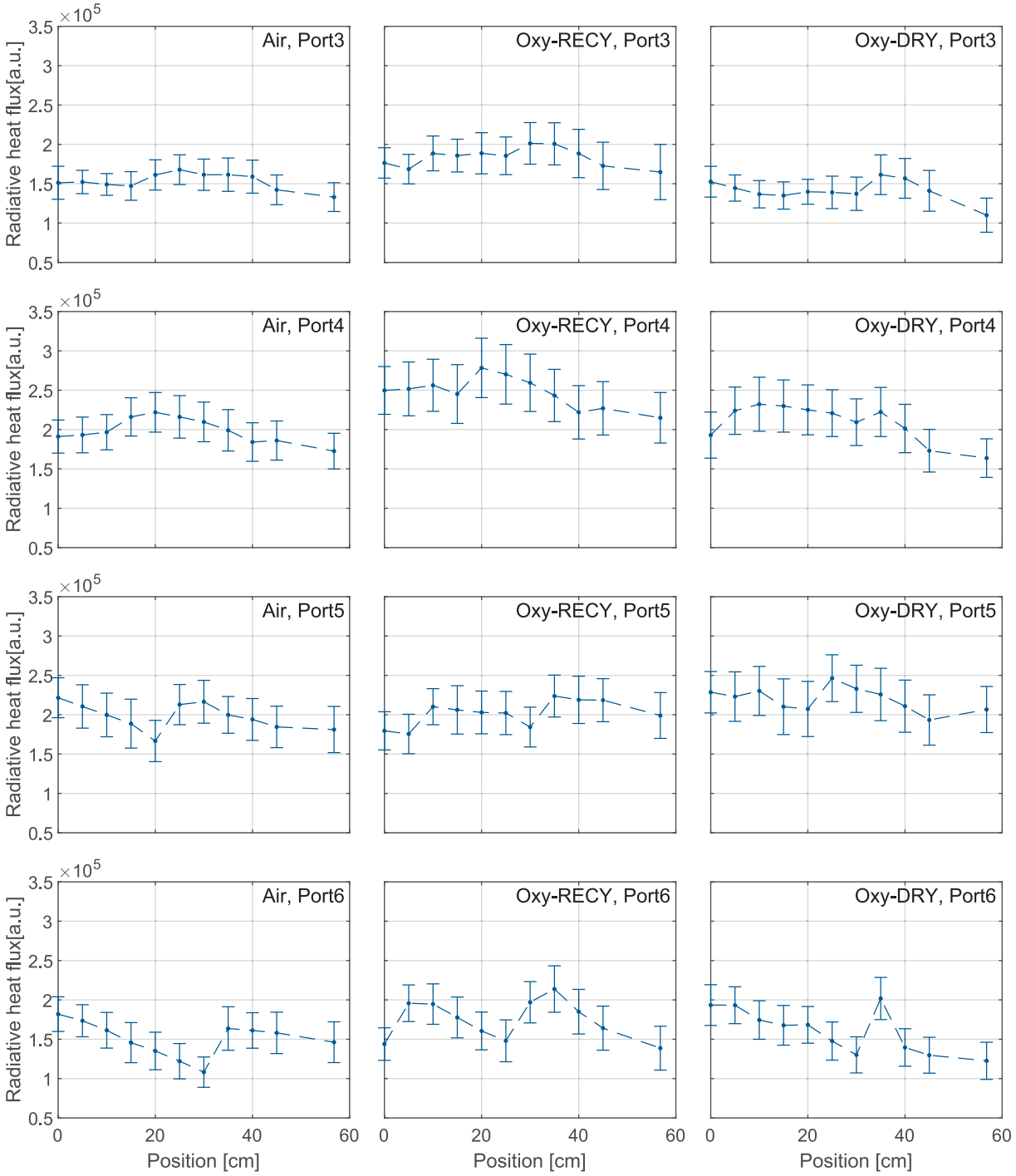

Fig. 13. Measured total radiative heat flux intensities of three different atmospheres (Air, Oxy-RECY, Oxy-DRY), four ports (3–6) and eleven axial positions.

the diagrams. Instead, to provide an impression of the result uncertainties, an exemplary spectrum obtained from the measurements at port 5 under Oxy-RECY conditions at the chamber wall is shown in Fig. 11.

Comparing all spectra shown in the figure, their overall shapes exhibit similar trends. In all datasets, pronounced and strongly fluctuating peaks can be observed, along with access-port dependent intensity levels. These features indicate that the measured spectra represent a superposition of thermal radiation emitted by burning particles and the chamber walls, as well as wavelength-specific radiation from the gaseous species present.

As observed in the previous section of the laminar flow reactor exhaust gas measurements, the peaks and fluctuations in the 2.5–3.5 μm range and above 4.8 μm can be attributed to water vapor emission lines [22], which have also been reported for flames in [26–29]. In addition, a small single peak at 3.33 μm is observed in all spectra and can be assigned to CH_4 emission lines [22,30]. This is consistent with expectations, as significant amounts of CH_4 are released during fuel pyrolysis [31–33]. Moreover, small fractions of natural gas were added to the flame feed gas under all operating conditions to stabilize the investigated flame and prevent blowouts, further contributing to the CH_4 content.

In the 4.1–5 μm range, the measured radiation spectra exhibit pronounced differences, which vary with the combustion atmosphere,

observation port, and probe insertion depth. Two stable peaks are observed at center wavelengths of 4.17 μm and 4.3–4.65 μm, while the center wavelength of the second peak shows port-dependent shifts and changes in shape. Between these two main peaks, the individual spectra differ considerably. For the air flame measurements at port 3 and a wavelength of 4.3 μm, the measured radiation intensities vary with measurement position, as displayed in Fig. 12.

For insertion depths of 0–15 cm, the spectra exhibit a consistent and well-defined local minimum. At greater insertion depths, this minimum increases, reaching a maximum at 40 cm, followed by a decrease towards the chamber center. Similar trends are also observed for the air flame at port 4 and for the two oxyfuel flames at ports 3 and 4. At ports 5 and 6, the local minimum of the air flame shows an inverse behavior. The highest heat fluxes occur at the chamber wall and center, while the lowest values are found at an insertion depth of 30 cm. In contrast, the spectra of the oxyfuel flames show no clear dependence of the local minimum on probe insertion depth and generally exhibit lower values than those observed for the air flame.

While Sun et al. [34] identified the peak at 4.17 μm as a CO emission line, the peaks in the 4.3–4.65 μm range have been attributed to CO_2 or CO emission bands [26–29]. The observed peak at 4.17 μm is, however, assumed to result from absorption effects caused by colder CO_2, as previously observed in the laminar flow reactor experiments. This interpretation is supported by the observed variations in the local minimum of the CO_2 emission intensities with respect to probe insertion depth and observation port. According to [22], CO would be expected to influence the spectrum in the 4.4–5.1 μm range. As no double peak is observed in this range for the air flame, the effect of CO is considered minor compared to that of CO_2. In contrast, in the two oxyfuel atmospheres, changes in the shape of the peak at 4.3–4.65 μm are evident. Compared to the air atmosphere, the peak tip appears more pointed, resulting from a dip in the lower-wavelength flank. Since the CO concentration in oxyfuel flames is known to be higher than in air flames [13,31,35,36], and the respective wavelengths of the dip corresponds to CO emission lines reported in [22], these observations are attributed to the presence of CO.

While the gas radiation peaks remain relatively constant, the differences in spectra at various radiometer insertion depths increase with distance from the burner head at ports 5 and 6. This is likely due to a more variable and broader flame geometry in this region, caused by turbulence and recirculation zones [25].

The overall radiative heat flux in the 2–5.5 μm wavelength range was calculated for each atmosphere, port, and insertion depth by summing the recorded radiation intensities across all wavelengths. A summary of the resulting data is shown in Fig. 13.

All radiative heat flux trends exhibit similar behavior, with the curves remaining relatively constant over insertion depth. However, for ports 3 and 4, a distinct trend is observed, since the flux initially slightly increases slightly with insertion depth, reaches a local maximum, and then decreases. This behavior is likely caused by complex and variable turbulent flame geometry [25]. It may also explain the increasing fluctuations observed at greater distances from the burner, from port 3 to 6, as the flame widens and becomes more unstable further downstream.

For all three flames, the overall radiative heat flux increases from port 3 to 4 (Air: 30 %, Oxy-RECY: 34 %, Oxy-DRY: 48 %, in average) and even to port 5 for Oxy-DRY (55 % in average) and then decreases towards port 6 (Air:24 %, Oxy-RECY: 29 %, Oxy-DRY: 26 %, in average), indicating the highest radiation intensity at approximately half the flame length, near the ports 4 and 5. Additionally, slightly higher fluxes are observed under oxyfuel conditions compared to the air atmosphere (Oxy-RECY: 16 %, Oxy-DRY: 4 % (all ports) or 8 % (ports 4–6), in average), consistent with the higher temperatures typically achieved in oxyfuel combustion [13,31,35,36].

5. Conclusion

A new radiometer concept is presented, combining the ellipsoidal cavity from conventional radiometers with fiber-optic radiation guiding for external detector application. This approach preserves the wavelength information of incident radiation and enables the use of external radiation analysis techniques. Characterization experiments, however, revealed the need for further optimization of the cavity geometry and surface quality.

Measurements were conducted for two different combustion scenarios: a small-scale laminar flow reactor under a methane oxy-fuel atmosphere, and walnut shell-fired semi-industrial solid fuel flames operated under three different air or oxyfuel conditions. The experiments demonstrated the general capability of the radiometer for flame characterization when coupled with a spectrometer.

The laminar flow reactor experiments highlighted the spectral capabilities of the system, providing clear representations of carbon dioxide and water vapor emission bands. In the semi-industrial swirl flame, the more complex flow structure and the presence of solid fuel particles lead to significant variations (up to 55 %) depending on operating conditions and measurement position. The observed relative intensity differences already provide a semi-quantitative mapping of the radiative field, which constitutes an important dataset for detailed flame characterization in this setup.

CRediT authorship contribution statement

L. Pörtner: Writing – original draft, Visualization, Validation, Software, Methodology, Investigation, Formal analysis, Data curation, Conceptualization. **B. Özer:** Writing – review & editing, Methodology, Investigation, Data curation, Conceptualization. **D. König:** Writing – review & editing, Investigation, Data curation. **M. Richter:** Investigation, Conceptualization. **M. Schiemann:** Writing – review & editing, Supervision, Resources, Project administration, Funding acquisition, Conceptualization. **A. Maßmeyer:** Supervision, Resources, Project administration, Funding acquisition, Conceptualization. **J. Ströhle:** Resources, Project administration, Funding acquisition. **B. Epple:** Supervision, Project administration, Funding acquisition.

Declaration of competing interest

The authors declare that they have no known competing financial interests or personal relationships that could have appeared to influence the work reported in this paper.

Acknowledgements

This work has been funded by the Deutsche Forschungsgemeinschaft (DFG, German Research Foundation) within the project SFB/TRR 129 “Oxyflame” (No. 215035359).

Data availability

Data will be made available on request.

References

[1] Tan Y, Croiset E, Douglas MA, Thambimuthu KV. Combustion characteristics of coal in a mixture of oxygen and recycled flue gas. Fuel 2006;85(4):507–12. https://doi.org/10.1016/j.fuel.2005.08.010.
[2] Richter M, König D, Ströhle J, Epple B. Radiative heat flux measurement in a semi-industrial oxyfuel combustion chamber with biomass and coal. Energies 2024;17(11):2735. https://doi.org/10.3390/en17112735.
[3] Smart JP, Patel R, Riley GS. Oxy-fuel combustion of coal and biomass, the effect on radiative and convective heat transfer and burnout. Combust Flame 2010;157(12):2230–40. https://doi.org/10.1016/j.combustflame.2010.07.013.

[4] Corrêa da Silva R, Krautz HJ. Experimental studies on heat transfer of oxy-coal combustion in a large-scale laboratory furnace. Appl Therm Eng 2015;82:82–97. https://doi.org/10.1016/j.applthermaleng.2015.02.045.
[5] Maßmeyer A, Zabrodiec D, Hees J, Kreitzberg T, Hatzfeld O, Kneer R. Flame pattern analysis for 60kWth flames under conventional air-fired and oxy-fuel conditions for two different types of coal. Fuel 2020;271:117457. https://doi.org/10.1016/j.fuel.2020.117457.
[6] Zabrodiec D, Massmeyer A, Hees J, Hatzfeld O, Kneer R. Flow pattern and behavior of 40 kWth pulverized torrefied biomass flames under atmospheric and oxy-fuel conditions. Renew Sustain Energy Rev 2021;138:110493. https://doi.org/10.1016/j.rser.2020.110493.
[7] Murthy AV, Wetterlund I, DeWitt DP. Characterization of an ellipsoidal radiometer. J Res Nat Inst Stand Technol 2003;108(2):115–24. https://doi.org/10.6028/jres.108.011.
[8] Gunnarsson A, Bäckström D, Johansson R, Fredriksson C, Andersson K. Radiative heat transfer conditions in a rotary kiln test furnace using coal, biomass, and cofiring burners. Energy Fuels 2017;31(7):7482–92. https://doi.org/10.1021/acs.energyfuels.7b00083.
[9] Tree DR, Tobiasson JR, Egbert SC, Adams BR. Measurement of radiative gas and particle emissions in biomass flames. Proc Combust Inst 2019;37(4):4337–44. https://doi.org/10.1016/j.proci.2018.06.221.
[10] Adams BR, Tobiasson JR, Egbert SC, Tree DR. Determining total radiative intensity in combustion gases using an optical measurement. Energy Fuels 2018;32(2):2414–20. https://doi.org/10.1021/acs.energyfuels.7b03290.
[11] Bäckström D, Johansson R, Andersson K, Wiinikka H, Fredriksson C. On the use of alternative fuels in rotary kiln burners — an experimental and modelling study of the effect on the radiative heat transfer conditions. Fuel Process Technol 2015;138:210–20. https://doi.org/10.1016/j.fuproc.2015.05.021.
[12] Bäckström D, Gall D, Pushp M, Johansson R, Andersson K, Pettersson JBC. Particle composition and size distribution in coal flames – the influence on radiative heat transfer. Exp Therm Fluid Sci 2015;64:70–80. https://doi.org/10.1016/j.expthermflusci.2015.02.010.
[13] Andersson K, Johansson R, Hjärtstam S, Johnsson F, Leckner B. Radiation intensity of lignite-fired oxy-fuel flames. Exp Therm Fluid Sci 2008;33(1):67–76. https://doi.org/10.1016/j.expthermflusci.2008.07.010.
[14] Andersson K, Johansson R, Johnsson F, Leckner B. Radiation intensity of propane-fired oxy-fuel flames: implications for soot formation. Energy Fuels 2008;22(3):1535–41. https://doi.org/10.1021/ef7004942.
[15] Johansson R, Gronarz T, Kneer R. Influence of index of refraction and particle size distribution on radiative heat transfer in a pulverized coal combustion furnace. J Heat Transfer 2017;139(4):42702. https://doi.org/10.1115/1.4035205.
[16] Kez V, Consalvi J-L, Liu F, Gronarz T, Ströhle J, Kneer R, et al. Investigation of gas and particle radiation modelling in wet oxy-coal combustion atmospheres. Int J Heat Mass Transf 2019;133:1026–40. https://doi.org/10.1016/j.ijheatmasstransfer.2019.01.013.
[17] Gorewoda J, Scherer V. Normal radiative emittance of coal ash sulfates in the context of oxyfuel combustion. Energy Fuels 2017;31(4):4400–6. https://doi.org/10.1021/acs.energyfuels.6b02866.
[18] Graeser P, Schiemann M. Char particle emissivity of two coal chars in oxy-fuel atmospheres. Fuel 2016;183:405–13. https://doi.org/10.1016/j.fuel.2016.06.116.
[19] Graeser P, Schiemann M. Emissivity of burning bituminous coal char particles – burnout effects. Fuel 2017;196:336–43. https://doi.org/10.1016/j.fuel.2017.01.110.
[20] Koch M, Pörtner L, Gu Y, Schiemann M, Rohlfs W, Kneer R. Comparison of scattering phase functions of reacting and non-reacting pulverised fuel particles. Fuel 2021;287:119415. https://doi.org/10.1016/j.fuel.2020.119415.
[21] Goldenstein CS, Miller VA, Mitchell Spearrin R, Strand CL. SpectraPlot.com: Integrated spectroscopic modeling of atomic and molecular gases. J Quant Spectrosc Radiat Transf 2017;200:249–57. https://doi.org/10.1016/j.jqsrt.2017.06.007.
[22] Gordon IE, Rothman LS, Hargreaves RJ, Hashemi R, Karlovets EV, Skinner FM, et al. The HITRAN2020 molecular spectroscopic database. J Quant Spectrosc Radiat Transf 2022;277:107949. https://doi.org/10.1016/j.jqsrt.2021.107949.
[23] Tarlinski D, Freisewinkel E, Eisenbach T, Span R, Schiemann M, Scherer V. Combustion of single walnut shell particles in a laminar flow reactor under oxy-fuel conditions: optical measurements and particle sampling. Fuel 2024;369:131613. https://doi.org/10.1016/j.fuel.2024.131613.
[24] Richter M, Ströhle J, Epple B. Up-scaling of a laboratory-scale pulverised oxyfuel burner to semi-industrial-scale through a flow similarity approach. Fuel 2024;371:131809. https://doi.org/10.1016/j.fuel.2024.131809.
[25] König D, Richter M, Ströhle J, Epple B. Stability and flame structure analysis of a semi-industrial swirl-stabilized oxy-fuel combustion chamber system for biomass. Energies 2025;18(6):1513. https://doi.org/10.3390/en18061513.
[26] Boulet P, Parent G, Acem Z, Kaiss A, Billaud Y, Porterie B, et al. Experimental investigation of radiation emitted by optically thin to optically thick wildland flames. J Comb 2011;2011:1–8. https://doi.org/10.1155/2011/137437.
[27] Boulet P, Parent G, Collin A, Acem Z, Porterie B, Clerc JP, et al. Spectral emission of flames from laboratory-scale vegetation fires. Int J Wildland Fire 2009;18(7):875. https://doi.org/10.1071/WF08053.
[28] Bourayou R, Vaillon R, Sacadura J-F. FTIR low resolution emission spectrometry of a laboratory-scale diffusion flame: experimental set-up. Exp Therm Fluid Sci 2002;26(2–4):181–7. https://doi.org/10.1016/S0894-1777(02)00125-5.
[29] Parent G, Acem Z, Lechêne S, Boulet P. Measurement of infrared radiation emitted by the flame of a vegetation fire. Int J Therm Sci 2010;49(3):555–62. https://doi.org/10.1016/j.ijthermalsci.2009.08.006.
[30] Thiévin J, Georges R, Carles S, Benidar A, Rowe B, Champion J-P. High-temperature emission spectroscopy of methane. J Quant Spectrosc Radiat Transf 2008;109(11):2027–36. https://doi.org/10.1016/j.jqsrt.2008.01.023.
[31] Ontyd C, Pielsticker S, Yildiz C, Schiemann M, Hatzfeld O, Ströhle J, et al. Experimental determination of walnut shell pyrolysis kinetics in N_2 and CO_2 via thermogravimetric analysis, fluidized bed and drop tube reactors. Fuel 2021;287:119313. https://doi.org/10.1016/j.fuel.2020.119313.
[32] Pielsticker S, Gövert B, Kreitzberg T, Habermehl M, Hatzfeld O, Kneer R. Simultaneous investigation into the yields of 22 pyrolysis gases from coal and biomass in a small-scale fluidized bed reactor. Fuel 2017;190:420–34. https://doi.org/10.1016/j.fuel.2016.10.085.
[33] Pielsticker S, Gövert B, Umeki K, Kneer R. Flash pyrolysis kinetics of extracted lignocellulosic biomass components. Front Energy Res 2021;9. https://doi.org/10.3389/fenrg.2021.737011.
[34] Sun H, Rong Z, Liu C, Liu J, Zhang Y, Zhang P, et al. Spectral characteristics of infrared radiation from forest fires. In: Gao W, Ustin SL, editors. Remote Sensing and Modeling of Ecosystems for Sustainability III. SPIE; 2006.
[35] Pielsticker S, Heuer S, Senneca O, Cerciello F, Salatino P, Cortese L, et al. Comparison of pyrolysis test rigs for oxy-fuel conditions. Fuel Process Technol 2017;156:461–72. https://doi.org/10.1016/j.fuproc.2016.10.010.
[36] Hjärtstam S, Andersson K, Johnsson F, Leckner B. Combustion characteristics of lignite-fired oxy-fuel flames. Fuel 2009;88(11):2216–24. https://doi.org/10.1016/j.fuel.2009.05.011.